THE JOURNAL OF PHYSICAL CHEMISTRY C
A JOURNAL OF THE AMERICAN CHEMICAL SOCIETY

Open Access
This article is licensed under CC-BY-NC-ND 4.0

Carbon-Mediated Oxygen Vacancy Creation at Hematite Interfaces

Frances E. Zengotita, Nabajit Lahiri, Mark H. Engelhard, Maksym Zhukovskyi, Manuel R. Vejar, Kevin M. Rosso, Carolyn I. Pearce,* and Amy E. Hixon*

Cite This: *J. Phys. Chem. C* 2025, 129, 7316−7326 Read Online

ACCESS | Metrics & More | Article Recommendations | Supporting Information

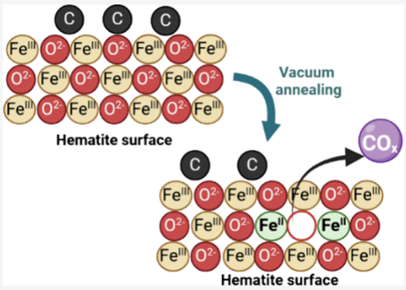

ABSTRACT: Nanoscale iron oxides (e.g., hematite (α-Fe_2O_3)) have unique properties, such as enhanced chemical reactivity and high surface area, when compared with their bulk counterparts. These nanoscale surfaces can be more reactive due to the presence of defects (e.g., oxygen vacancies). In this work, we probed the surface chemistry of bulk and nanoscale hematite via X-ray photoelectron spectroscopy, electron microscopy, and powder X-ray diffraction. Oxygen exposure and vacuum annealing experiments were conducted to add or remove oxygen vacancies and remove adventitious carbon. In the absence of the oxygen annealing step, vacuum annealing resulted in partial reduction of Fe(III) to Fe(II) on all hematite surfaces. This is a size-dependent effect, with the extent of reduction increasing as the crystallite size decreases. In addition, the atomic concentrations of carbon increased on all iron oxide surfaces after vacuum annealing. Oxygen annealing almost completely removed carbon from sample surfaces, and no Fe(III) reduction was observed in the absence of carbon. Under these conditions, the results reveal that carbonaceous material enhances oxygen vacancy formation, which then facilitates the reduction of Fe(III) on hematite surfaces. We provide new insights into the mechanisms of Fe(III) reduction on both bulk and nanoscale hematite surfaces and establish the major role of carbon in oxygen vacancy formation.

INTRODUCTION

Nanoparticles have at least one dimension that measures 1−100 nm and are known for having interfacial properties that are strongly dependent on size, shape, and chemical composition.[1−5] These interfacial properties can impact the electronic and crystal structure of the material and affect solubility and adsorption behavior.[1] In general, as a material's dimensions decrease from bulk to nanoscale, the surface area to volume ratio and surface energy increases,[1,2,6] which results in a larger number of undercoordinated atoms at the nanoparticle surface.[1,7] These structural changes can result in changes to surface stoichiometry and enhance structural disorder.[6] In iron oxide nanoparticles, the redox potential of surface Fe becomes size dependent, which affects the proton-affinity of coordinating oxygen atoms.[1,6,8]

Hematite (α-Fe_2O_3) is an iron oxide semiconductor (band gap ≈ 2.1 eV) that can be thermodynamically stable under some atmospheric conditions and exhibits a unique chemical reactivity.[8−11] At the nanoscale, hematite demonstrates size-dependent effects that can impact the redox chemistry, sorption affinity, and chemical behavior of metal contaminants; distorted binding environments and undercoordinated site reactivity are important considerations.[2,6,9] Crystallite size can impact both the stoichiometry and structure of hematite, which can cause local phase transitions.[8,9,12]

Oxygen vacancies can play a major role in dictating the properties of nanoparticles.[10,13−15] Oxygen vacancies can act as shallow donor dopants, and their creation may increase the overall carrier electron concentration.[13,16,17] Oxygen vacancies can also impact the conductivity of hematite by facilitating the reduction of Fe(III) to Fe(II) due to the introduction of up to two electrons.[13,16] Investigations on defects in the structure of hematite reveal that oxygen vacancy concentrations can lead to local phase transitions (e.g., hematite (α-$Fe^{III}{}_2O_3$) to magnetite ($Fe^{II,III}{}_3O_4$)) under certain conditions.[12,13,18] Oxygen vacancies can also induce surface reduction with hematite nanoparticles and films.[10,13] However, knowledge gaps still exist on surface reduction with oxygen vacancies with respect to crystallite size, surface impurities and mineral complexity. To address these knowledge gaps, the presented study probes multifaceted hematite surfaces as a function of crystallite size under various conditions to provide valuable insights on surface reduction.

The purpose of the present study is to use X-ray photoelectron spectroscopy, electron microscopy and X-ray diffraction, to investigate multifaceted hematite surfaces as a function of crystallite size under varying conditions. Vacuum and oxygen annealing conditions served to create or remove oxygen vacancies and remove carbon from the mineral surfaces, which resulted into the changes to the near-surface composition of the particles.

Received: December 12, 2024
Revised: March 18, 2025
Accepted: March 31, 2025
Published: April 7, 2025

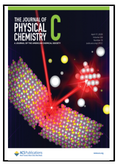

ACS Publications

© 2025 The Authors. Published by American Chemical Society

https://doi.org/10.1021/acs.jpcc.4c08423

■ METHODS

Synthesis and Characterization. Bulk hematite was purchased from Sigma-Aldrich (≥96% iron(III) oxide with a particle size of <5 μm) and used as received. NH08 was synthesized by adapting the method of Madden et al.[8] Briefly, 60 mL of 1.0 M $Fe(NO_3)_3(aq)$ was added dropwise to 750 mL of boiling deionized water (18.2 MΩ·cm at 25 °C) under constant stirring. The suspension was removed from the heat after a color change indicated that all the $Fe(NO_3)_3(aq)$ had been consumed; it was left to cool overnight. After cooling, the suspension was transferred to dialysis tubing (2 kDa, Repligen Spectra, Spectrum Laboratories) that was submerged in deionized water for 2 weeks. NH40 was synthesized according to the method of Voelz et al.[19] One liter of 0.002 M $HNO_3(aq)$ (ACS Reagent grade) was heated overnight at 98 °C. $Fe(NO_3)_3 \cdot 9H_2O(s)$ (8.08 g) was added and the solution was stirred to facilitate complete dissolution before the solution was returned to the oven and heated at 98 °C for 7 days. The resulting red suspension was transferred to dialysis tubing and submerged in deionized water for 2 weeks.

All suspensions were placed in separate Falcon conical centrifuge tubes (50 mL) and were separated and centrifuged (Eppendorf) at 14,000 rpm for 1–2 h. The supernatant was removed from the centrifuge tubes, leaving a wet red solid at the bottom of the vessel. The conical centrifuge tubes were then transferred to a freeze-dryer (Labconco, FreeZone Freeze-Dryer XL). Each freeze-drying session was conducted based on crystallite size (one session for NH08 and another separate session for NH40) to prevent any potential sample contamination. The samples were placed into the drying chamber and then freeze-dried at ≤ -40 °C and in vacuum at ≤ 0.133 mbar. The freeze-dried nanoparticle powder samples were then used for the experiments.

Powder X-ray Diffraction. Prior to treatment, samples were drop-cast onto a glass slide and left to dry in air. Analyses were conducted on a Bruker D8 Discover diffractometer equipped with Cu Kα radiation (λ = 1.541 Å) and a LynxEye solid-state pixel detector. Data was collected from 15–80 °2θ with a step size of 0.02° and a scan rate of 15 s per step. Vacuum annealed samples were removed from the XPS chamber under $N_2(g)$ and transferred to glass scintillation vials. PXRD patterns for vacuum annealed samples were collected with Cu Kα radiation (λ=1.5418 Å) using a Rigaku Miniflex II diffractometer, operated at 30 kV and 15 mA. Data were collected between 3 and 90 °2θ, using a scan width of 0.04° and a 5-s count time. Simulated mineral patterns were produced using CrystalDiffract© (CrystalMaker Software Ltd., Oxford, England (www.crystalmaker.com) from published CIF patterns.[20−22] Rietveld refinement analyses were performed using Profex, a graphical user interface for Rietveld refinement analyses.[23]

Scanning and Transmission Electron Microscopy. Scanning electron microscope images were collected on a JEOL JCM-6000 Plus Neoscope Benchtop SEM at accelerating voltages from 10 to 15 kV. Secondary electron mode was used to conduct morphological analyses of bulk hematite. ImageJ[24] was used to determine the size distribution based on measurements of at least 100 crystallites from different regions of the sample (see Figure S1 and Table S1). High resolution transmission electron microscopy (HR TEM), selected area electron diffraction (SAED), and scanning transmission electron microscopy (STEM) were performed on a Talos F200i (S)TEM (Thermo Scientific) field emission transmission electron microscope operating at 80–200 kV accelerating voltages.

Surface Area Analysis. The structural properties of the hematite samples were determined using $N_2(g)$-BET and calculated using the BJH and HK models. For the surface area analysis, 100 mg of each sample was placed in the degas port at 100 °C for 24 h prior to $N_2(g)$ isotherm analysis at 77 K on a Micromeritics ASAP2020 physisorption analyzer. Results are provided in SI as Table S1.

X-ray Photoelectron Spectroscopy. XPS measurements were performed with a Physical Electronics Quantera SXM Scanning X-ray Microprobe. This system uses a focused monochromatic Al Kα X-ray (1486.7 eV) source for excitation and a spherical section analyzer. The instrument has a 32-element multichannel detection system. The X-ray beam is incident normal to the sample and the photoelectron detector is at 45° off-normal. High energy resolution spectra were collected using a pass-energy of 69.0 eV with a step size of 0.125 eV. For the Ag $3d_{5/2}$ line, these conditions produced a fwhm of 0.92 ± 0.05 eV. The binding energy scale was calibrated using the Cu $2p_{3/2}$ feature at 932.62 ± 0.05 eV and Au $4f_{7/2}$ at 83.96 ± 0.05 eV. Low energy electrons at ∼ 1 eV, 20 μA and low energy Ar^+ ions were used to minimize sample charging during analysis. XPS data was processed using CasaXPS software using a Shirley background approximation and Gaussian–Lorentzian lineshapes. Spectra was charge referenced using the O 1s (lattice oxide component) at 530 eV.

Vacuum Annealing Experiments (VAC). Iron oxide samples were deposited into a 20 mm × 30 mm sample heating block. The Cu block is fixed with internal heating elements and a type K thermocouple electrically isolated with sapphire. The entire sample heating/cooling holder is compatible with the Physical Electronics vacuum sample stage and transfer arm and controlled using a PHI model 20–300 Hot/Cold Module Control, Eurotherm temperature controller, and DC power supply. The samples were then transferred under a vacuum into the attached Applied Testing Systems Model 3210 quartz tube vacuum furnace and Quantera XPS analysis chamber. The samples were vacuum annealed at 300 °C and $<5 \times 10^{-7}$ Torr for 1 h. Full sets of core-level spectra, including Fe 3p, O 1s, C 1s, Fe 2p, and valence band, were acquired prior to and after vacuum annealing.

Oxygen + Vacuum Annealing Experiments (OAE-1). NH08 was drop-casted onto a clean ∼ 1 cm^2 Si wafer, which was mechanically secured to a small 0.5-in. diameter quartz tube heating stub and transferred under vacuum into the attached Applied Testing Systems Model 3210 quartz tube vacuum furnace and Quantera XPS analysis chamber. The quartz tube was filled with ultrahigh pressure $O_2(g)$ to 100 mTorr and heated at 10 °C·min^{-1} to 350 °C, held at 350 °C for 1.5 h, then cooled to room temperature in $O_2(g)$. The sample was then transferred under vacuum into an attached nitrogen glovebox (<1 ppm of O_2 and H_2O). The sample was removed from the 0.5-in. diameter quartz tube heating stub and remounted onto the 20 mm × 30 mm Cu sample heating block. The heating block was transferred under vacuum back into the quartz furnace to be vacuum annealed at ∼ 250 °C for 1 h. An additional vacuum annealing step was conducted at 300 °C for 110 min. Both vacuum annealing steps were conducted at $<5 \times 10^{-7}$ Torr.

Oxygen + Vacuum Annealing Experiments (OAE-2). All three iron oxide samples (Bulk, NH40, and NH08) were placed in the Cu heating block and transferred to the quartz tube vacuum furnace attached to the Quantera XPS analysis chamber.

The first oxygen annealing was performed at 100 mTorr in $O_2(g)$ and heated incrementally at a rate of 10 °C·min^{-1} until 300 °C was reached and then held for 1 h. After the first step was completed, an additional oxygen annealing step was conducted at 100 mTorr in $O_2(g)$ and heated to 350 °C at a rate of 10 °C·min^{-1}. Subsequently, the samples were vacuum annealed at a rate of 10 °C·min^{-1} to 300 °C at $<5 \times 10^{-7}$ Torr in a quartz furnace.

■ RESULTS AND DISCUSSION

Nanoparticle characterization is challenging because size-dependent effects are difficult to quantify when using traditional approaches, especially at diameters smaller than 10 nm.[8,9,12,25−28] For example, peak broadening is observed in powder X-ray diffractograms, and electron beams from high-resolution transmission electron microscopy (HR TEM) can damage the sample, which impacts electron diffraction and lattice spacing measurements.[26] Because of these challenges, we complemented traditional characterization with X-ray photoelectron spectroscopy (XPS). Experimental conditions of this work are provided below. Vacuum annealing was used to induce oxygen vacancies and oxygen annealing was used to remove carbon from the surface of hematite samples (Table 1).

Table 1. Experimental Conditions for XPS Experiments[a]

sample	experiment designation	treatment 1	treatment 2	treatment 3
NH08	VAC	300 °C in vacuum 1 h		
NH40	VAC	300 °C in vacuum 1 h		
bulk	VAC	300 °C in vacuum 1 h		
NH08	OAE-1	350 °C at 0.1 Torr O_2 1.5 h	250 °C in vacuum 1 h	300 °C in vacuum 1.75 h
NH08	OAE-2	300 °C at 0.1 Torr O_2 1 h	350 °C at 0.1 Torr O_2 1.5 h	300 °C in vacuum 1 h
NH40	OAE-2	300 °C at 0.1 Torr O_2 1 h	350 °C at 0.1 Torr O_2 1.5 h	300 °C in vacuum 1 h
bulk	OAE-2	300 °C at 0.1 Torr O_2 1 h	350 °C at 0.1 Torr O_2 1.5 h	300 °C in vacuum 1 h

[a] NH08 = nano-hematite with a diameter of 8 nm; NH40 = nano-hematite with a diameter of 40 nm; bulk = bulk hematite. VAC = vacuum annealing experiment, OAE = oxygen + vacuum annealing experiment.

Vacuum Annealing Experiments (VAC). *Powder X-ray Diffraction (PXRD).* Vacuum annealing (VAC) was performed as described in Table 1. Bulk hematite, NH40, and NH08 were characterized via powder X-ray diffraction (PXRD), electron microscopy (EM), and X-ray photoelectron spectroscopy (XPS). Prior to vacuum annealing treatment, the samples were characterized via PXRD and Rietveld refinement. All Brag peaks of XRD patterns showed only hematite reflections, indicating that the main phase was α-Fe_2O_3. Thus, the samples were found to be hematite (100%) prior to vacuum annealing (Figure 1 and Table S2). The PXRD results are displayed in Table 2 for all starting materials before vacuum annealing. Small shifts in d-spacings for NH08 due to an amorphous contribution from the substrate or specimen displacement cannot be ruled out due to the texture and amount of material used for analysis. Fe site occupancies, Fe_{occ}, can be determined by the ratio between the (214) and (300) peaks in the hematite PXRD pattern.[29] Fe_{occ} varied across crystallite sizes where NH08 had an $Fe_{occ} = 0.87$ and larger crystallite sizes had greater $Fe_{occ} \geq 0.98$. This finding suggests that NH08 is Fe-deficient in comparison to larger crystallite sizes prior to vacuum annealing.[29] The Fe_{occ} for NH08 changes to ≥ 0.98 after vacuum annealing, which suggests that NH08 is no longer Fe-deficient.

All samples remained crystalline after vacuum annealing (Figure 1), which is not surprising given that thermal annealing is known increase and improve crystallinity in solids.[30−32] This improvement in crystallinity and structure is unique to NH08, whose Fe deficiencies improved after vacuum annealing. Further, the increase in Fe_{occ} can be interpreted as NH08 becoming more like stochiometric hematite.[29,33]

The XRD patterns for NH08 and NH40 vacuum annealed samples showed an increase in the intensity of reflections associated with partially oxidized magnetite along the magnetite-maghemite solid solution (Fe_3O_4−$Fe_{8/3}O_4$). Magnetite has a unit cell length (a) of 8.396−8.400 Å but, as it oxidizes, the unit cell becomes smaller due to the smaller atomic size of Fe(III) and the formation of vacancies, with fully oxidized maghemite having a unit cell length (a) of 8.33−8.34 Å.[34] Rietveld refinement results after vacuum annealing (Figures S2−S4, Table S3) show that bulk hematite contained 98.8 ± 0.24% hematite and 1.18 ± 0.48% magnetite/maghemite; NH40 contained 91.4 ± 0.35% hematite and 8.58 ± 1.38% magnetite/maghemite; and NH08 contained 62.2 ± 0.85% hematite and 37.8 ± 1.84% magnetite/maghemite. The Rietveld refinement results ultimately suggest that the samples after vacuum annealing are hematite with a magnetite-maghemite solid

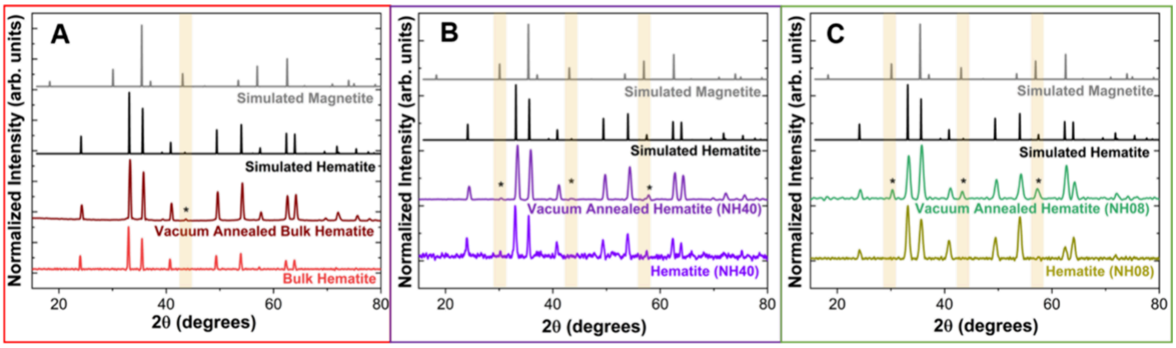

Figure 1. Powder X-ray diffractograms before and after vacuum annealing (VAC): (A) bulk hematite; (B) NH40; and (C) NH08. Simulated magnetite and hematite patterns are based on published patterns.[20−22] Highlighted regions and asterisks show the contribution of magnetite to the hematite samples. Note: The colored boxes represent the type of sample; bulk hematite as red, NH40 as purple and NH08 as green.

Table 2. PXRD Results for All Hematite Samples before and after Vacuum Annealing (VAC) Experiments

	before vacuum annealing		after vacuum annealing		
sample	*d*-spacing (Å)	*hkl*	*d*-spacing (Å)	*hkl*	mineral phase
NH08	3.685	(012)	3.649	(012)	hematite
	2.704	(104)	2.948	(220)	magnetite/maghemite
	2.513	(110)	2.685	(104)	hematite
	2.209	(113)	2.505	(311), (110)	magnetite/maghemite, hematite
	1.842	(024)	2.188	(113)	hematite
	1.695	(116)	2.088	(400)	magnetite/maghemite
	1.593	(018)	1.832	(024)	hematite
	1.485	(214)	1.689	(422), (116)	magnetite/maghemite, hematite
	1.453	(300)	1.606	(511), (018)	magnetite/maghemite, hematite
	1.315	(1010)	1.480	(440), (214)	magnetite/maghemite, hematite
	1.259	(220)	1.449	(300)	hematite
			1.309	(1010)	hematite
			1.277	(533)	magnetite/maghemite
NH40	3.715	(012)	3.649	(012)	hematite
	2.711	(104)	2.939	(220)	magnetite/maghemite
	2.527	(110)	2.677	(104)	hematite
	2.209	(113)	2.499	(311), (110)	magnetite/maghemite, hematite
	1.845	(024)	2.193	(113)	hematite
	1.697	(116)	2.074	(400)	magnetite/maghemite
	1.606	(018)	1.832	(024)	hematite
	1.492	(214)	1.687	(422), (116)	magnetite/maghemite, hematite
	1.454	(300)	1.594	(511), (018)	magnetite/maghemite, hematite
	1.316	(1010)	1.480	(440), (214)	magnetite/maghemite, hematite
	1.258	(220)	1.447	(300)	hematite
			1.307	(1010)	hematite
			1.276	(533)	magnetite/maghemite
bulk	3.710	(012)	3.664	(012)	hematite
	2.715	(104)	2.693	(104)	hematite
	2.529	(110)	2.505	(311), (110)	magnetite/maghemite, hematite
	2.215	(113)	2.203	(113)	hematite
	1.848	(024)	2.074	(400)	magnetite/maghemite
	1.701	(116)	1.839	(024)	hematite
	1.607	(018)	1.692	(422), (116)	magnetite/maghemite, hematite
	1.490	(214)	1.596	(511), (018)	magnetite/maghemite, hematite
	1.456	(300)	1.484	(440), (214)	magnetite/maghemite, hematite
	1.314	(1010)	1.451	(300)	hematite
	1.261	(220)	1.310	(1010)	hematite
			1.257	(220)	hematite

solution series (which is commonly referred to partially oxidized magnetite).[34] This change in phase from hematite to oxidized magnetite (maghemite) is expected, as the vacuum annealing process can reduce Fe(III) to Fe(II).[13,18,35−37]

The PXRD and Rietveld refinement results show that the extent of hematite reduction is size dependent. The extent of reduction followed the trend NH08 > NH40 > Bulk, with increased *d*-spacings corresponding to formation of phases that were closer to the magnetite end of the solid solution at smaller crystallite sizes. Wang et al.[38] report a solid phase transformation from akaganéite to a maghemite/magnetite phase as a result from high pressure (i.e., vacuum heating $>10^{-7}$ mbar) and also report a size-dependent transformation from akaganéite to maghemite. Another study led by Karim et al.[39] probed the extent of oxidation of iron oxide nanoparticles and evaluated the size-dependent redox behavior of iron via spectro-microscopy. The study showed that there was a greater extent of oxidation with the smaller nanoparticles, which they attribute to smaller crystallite sizes having more structural disorder and less commensurate interfaces between crystallites which enhances diffusion of vacancies and iron cations.[39] Similarly, we propose that the structural disorder and high reactive surface area at smaller crystallite sizes may play a role in the transformation of hematite to maghemite/magnetite in this study.

Transmission Electron Microscopy. To further investigate these changes in the crystalline structure, we conducted high-resolution TEM (HR TEM) and electron diffraction analyses on vacuum annealed NH40 and NH08. We focus here on the results for NH08, but equivalent information is provided in Figure S5−S6 and Table S4−S5 for NH40. HR TEM analysis was conducted on four different locations of the NH08 sample to determine the crystalline phase(s) (Figure 2). The HR TEM analyses (Figure 2**A**) revealed *d*-spacings that suggest the presence of multiple crystalline phases (e.g., hematite, maghemite, and magnetite). Area #1 aligned with the hematite (012) plane (d = 0.36 nm), Area #3 aligned with magnetite (111) plane (d = 0.48 nm), and Area # 2 and Area #4 aligned with the hematite (104) plane (d = 0.27 nm).[9,10] In addition, we observed voids in NH08 and NH40 (Figure S7) that may have been induced by the vacuum annealing treatment.[40] These voids were likely created by temperature-induced stress and the condensation of oxygen vacancies at the surface of the materials.[41,42] Although other studies have found that electron beam irradiation may cause the formation of voids,[43] we did not observe void formation even after allowing the electron beam to dwell on a vacuum annealed sample for 5−10 min. No inclusions were found in the voids via HR TEM analyses. Additional electron microscopy imaging is available in the SI file (Figures S8−S10).

NH08 displays a distorted lattice based on the electron diffraction results, with a smaller *d*-spacing (Figure 2**B**, Table 3, and Figure S11) for the starting material than would be expected for bulk hematite, i.e., ∼ 3.4 Å versus ∼ 3.6−3.7 Å for the (012) crystal plane,[44] which may be a result of lattice distortions or structural defects.[6,45] Similarly, Souza et al.[45] report a decrease in *d*-spacing in the electron diffraction results as structural defects increase in 2-line ferrihydrite due to Al-substitution. Although the PXRD results (Figure 1) show that the bulk structure of NH08 aligns with hematite, at nanoscale, there may be defects in the structure which results in a decrease in *d*-spacing. To our knowledge, no other study reports a smaller *d*-spacing for hematite nanoparticles for electron diffraction. After vacuum annealing, NH08 is polycrystalline (Figure 2**C**) and the *d*-spacing is consistent with larger hematite crystallite sizes (Table 3, Figure S12). These changes can be attributed to the increase in grain size after annealing treatment.[46] After vacuum annealing, the mobility of surface adatoms is increased, which leads to the coalescence of small grains into larger grains with improved crystallinity.[46] Annealing improves crystallinity,[47] increases crystallite size,[48] and likely removes the lattice distortions in the NH08 starting material.

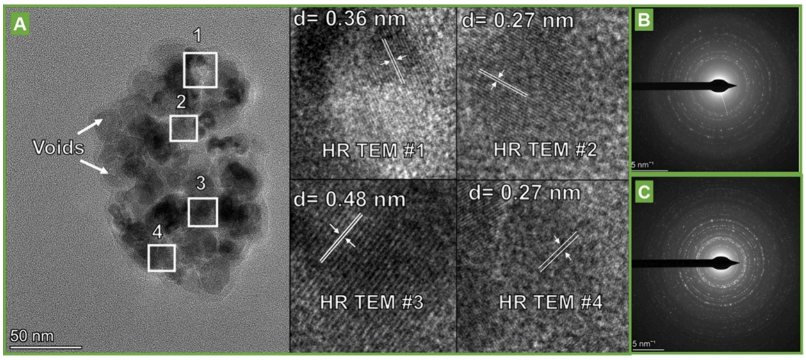

Figure 2. (A) Transmission electron microscopy (TEM) image and high resolution transmission electron microscopy (HR TEM) analyses of NH08 after vacuum annealing (VAC). (B) Electron diffraction prior to vacuum annealing. (C) Electron diffraction of NH08 after vacuum annealing.

Table 3. Crystal Plane Spacing Calculated from the Electron Diffraction of NH08 before and after Vacuum Annealing (VAC)[a]

sample	d-spacing$_{\text{before}}$ (Å)	d-spacing$_{\text{after}}$ (Å)	hkl_{after}	mineral phase$_{\text{after}}$
NH08	3.452	4.861	(111)	magnetite
	2.563	3.755	(012)	hematite
	2.338	2.974	(220)	magnetite/maghemite
	2.077	2.754	(104)	hematite
	1.736	2.581	(311), (110)	magnetite/maghemite, hematite
	1.612	2.239	(113)	hematite
	1.407	2.124	(400)	magnetite/maghemite
	1.250	1.877	(024)	hematite
		1.729	(422), (116)	magnetite/maghemite, hematite
		1.630	(511)	magnetite/maghemite
		1.487	(440), (214)	magnetite/maghemite, hematite
		1.337	(620), (1010)	magnetite/maghemite, hematite

[a] The subscript "before" represents the d-spacing values and hkl of the starting material prior to vacuum annealing, whereas the subscript "after" represents the d-spacing values and hkl of NH08 after vacuum annealing. Due to the potentially distorted lattice of NH08, hkl_{before} values are not reported and assigned.

The diversity in d-spacings in Table 2 and Table 3 confirm that partial reduction of hematite nanoparticles to a phase along the magnetite-maghemite (Fe_3O_4−$Fe_{8/3}O_4$) solid solution occurs after vacuum annealing. Complete phase transitions to magnetite or another Fe(II)-bearing mineral surface would be expected at higher temperatures (≥350 °C).[10,13,18,35,49] Oxygen vacancies, when present in sufficient concentration, reduce Fe(III) to Fe(II),[13] which can lead to an eventual phase transition to Fe_3O_4−$Fe_{8/3}O_4$.[13,35,50] Thus, partial reduction may have been caused by a high concentration of oxygen vacancies.[13,35]

X-ray Photoelectron Spectroscopy (XPS). The effect of oxygen exposure and vacuum annealing on the hematite samples was investigated by surface sensitive XPS; survey scans can be found in the SI (Figure S13−S15). The C 1s region (Figure 3) and the survey spectra (Table S6) showed that the carbon content of all three samples increased to 25−30% after vacuum annealing. Additionally, the type of carbon changed from typical adventitious carbon to amorphous carbon after annealing.[51−53] Build-up of adventitious carbon species from the atmosphere is typical of air-exposed samples.[54] The impact of sample storage environments and long beam exposures in the reduction of carbon species over time can contribute to carbon accumulation.[53,55,56] The increase in carbon at the surface after vacuum annealing may be due to the carbon coming from the pores of the material, given that the sample is a powder pellet. In addition, the changes in carbon speciation may be due to either the loss of oxygen functional groups (e.g., O−C−O, CO_3)[57] or potential dehydrogenation[58] after vacuum annealing. Carbon species (e.g., esters, carbonates, and carbonyls) were identified through fitting of the C 1s spectra in CasaXPS using line shapes with 70% Gaussian and 30% Lorentzian contributions.[59] Additional XPS fitting (i.e., O 1s) and parameters are described in the SI (Figure S16 and Table S7).

Three major conclusions can be drawn by comparing the C 1s region spectra collected before vacuum annealing (Figure 3**A**−**C**, top row) and after vacuum annealing (Figure 3**D**−**F**, bottom row): (1) C = C conjugation was apparent at ∼ 284.4 eV; (2) the π−π* satellite (∼290 eV) appeared; and (3) there were changes to C = O concentration at the surface (288−290 eV). There is a change in speciation after vacuum annealing, as indicated by the decrease in the intensity of the C−C peak at 285 eV and an increase in the intensity of the C = C peak at 284.4 eV. This change in speciation suggests that surface carbon becomes more graphitic.[60,61] In addition, there is also a decrease in the intensity of the carbonate peak, which may be due to a decrease in carbonate species (∼289.3 eV), with studies reporting an increase in temperature in ultrahigh vacuum can lead to the removal of carbonate.[62−64] During the thermal annealing of graphene oxide, the sp^2 carbon fraction increases with increasing vacuum annealing temperature due to the removal of oxygen functional groups,[57] as evidenced by the narrowing of the sp^2-C peak in the XPS C 1s core-level spectra.[65] The sp^2-hybridized carbon is a good indicator of graphitization in carbonaceous material after vacuum annealing.[65]

Fe 2p spectra provide insight into the oxidation state at the hematite surface before and after vacuum annealing.[66] For example, Fe 2$p_{3/2}$ core-level lines for α-Fe_2O_3 (an Fe(III) compound), Fe_3O_4 (a mixed Fe(II) and Fe(III) compound), and FeO (an Fe(II) compound) occur at 711.0, 710.3, and 710.0 eV, respectively,[35] and there is a well-known Fe(III) satellite around 719 eV (∼8.5 eV above the main peak).[35] The Fe 2p spectra for bulk hematite, NH40, and NH08 showed an increase in Fe(II) content after vacuum annealing (Figure 4**A**−**C**). The Fe 2$p_{3/2}$ and Fe 2$p_{1/2}$ peaks broadened and shifted to lower binding energy and there was a decrease in the intensity of the Fe(III) satellite.[10,35] The Fe(III) satellite intensity decreased

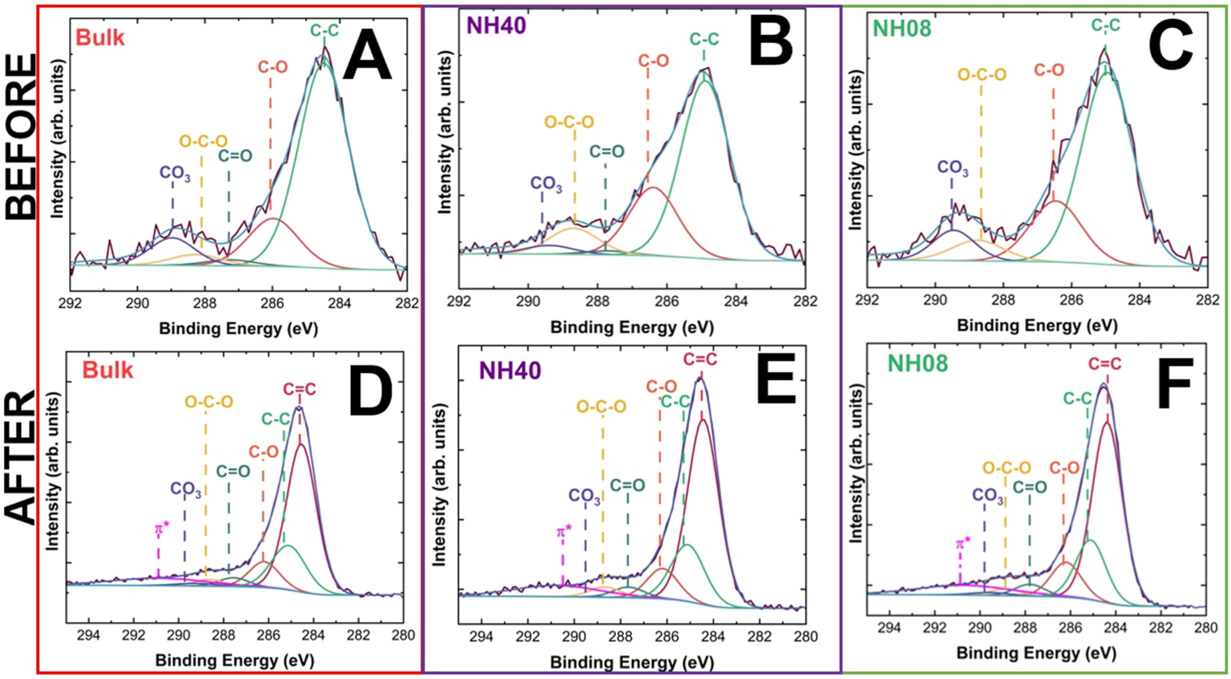

Figure 3. C 1*s* core-level X-ray photoelectron spectra. Panels (A−C) show the carbon content and speciation before vacuum annealing, and panels (D−F) show the carbon content and speciation after vacuum annealing (VAC). The colored boxes represent the type of sample; bulk hematite as red, NH40 as purple and NH08 as green.

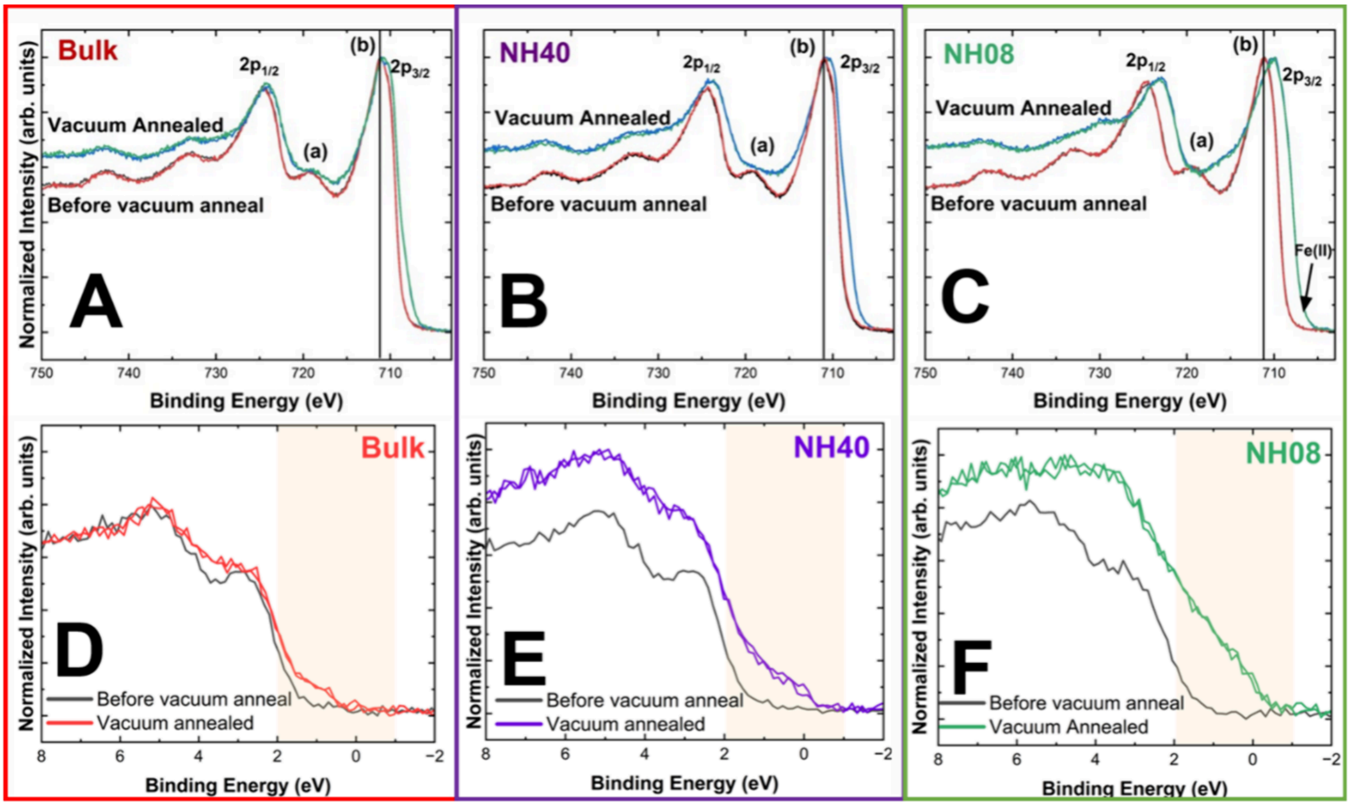

Figure 4. Selected XPS core-level spectra of samples before and after vacuum annealing (VAC): (A) bulk hematite Fe 2*p* core-level spectra; (B) NH40 Fe 2*p* core-level spectra; (C) NH08 Fe 2*p* core-level spectra; (D) bulk hematite valence band; (E) NH40 valence band; (F) NH08 valence band. (a) Location of the Fe(III) satellite and (b) Fe $2p_{3/2}$ peak position prior to vacuum annealing. Spectra were collected on two separate areas (one spectrum per area) of the sample surface and are displayed together to highlight any differences at the mineral surface (Fe 2*p* and valence band). The colored boxes represent the type of sample; bulk hematite as red, NH40 as purple, and NH08 as green.

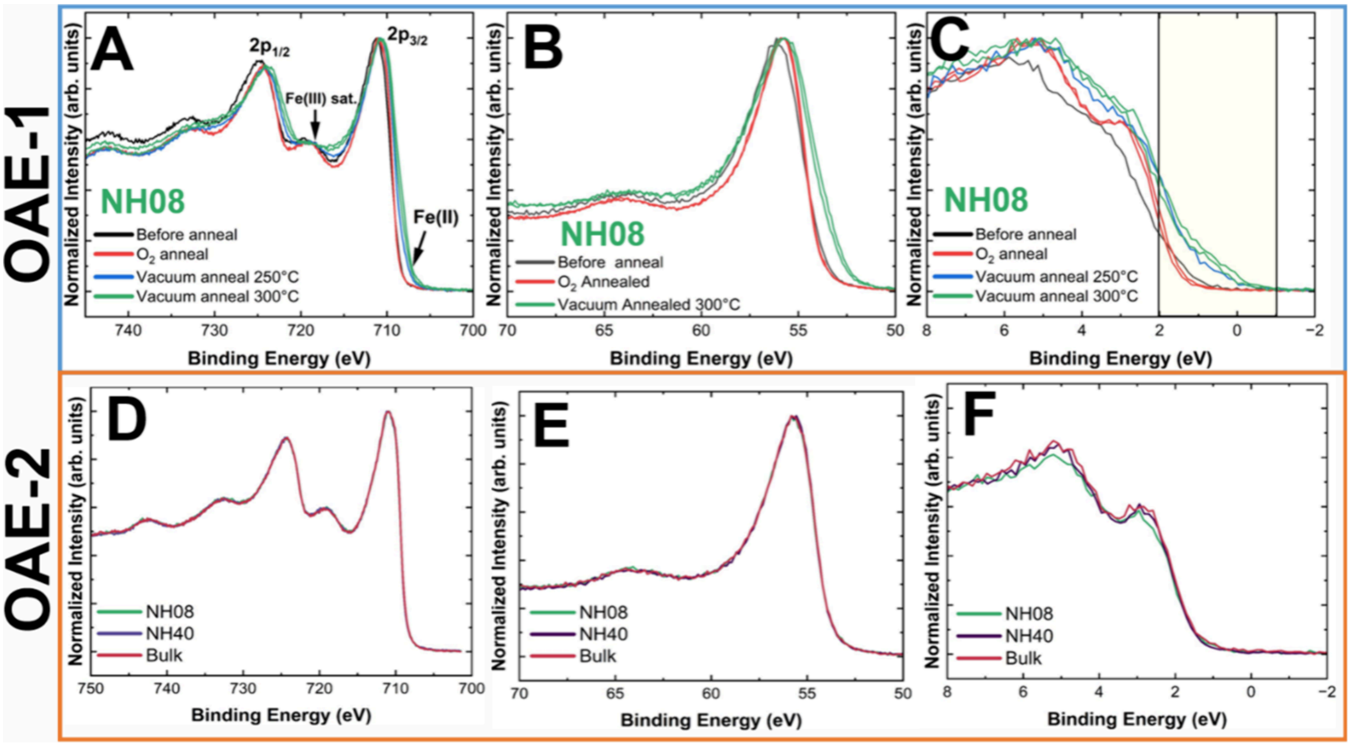

Figure 5. Comparison of the X-ray photoelectron spectra for NH08 (OAE-1) as (A−C); X-ray-photoelectron core-level spectra of all samples (OAE-2) as (D−F) where (D) Fe 2*p* core-level spectra, (E) Fe 3*p* core-level spectra, and (F) valence band spectra. OAE-1 represents an experiment where some carbon was removed at the surface due to one oxygen annealing step followed by two vacuum annealing steps. OAE-2 represents a second, separate experiment where the carbon was nearly completely removed from sample surfaces due to two oxygen annealing steps followed by one vacuum annealing step. Spectra were collected on two separate areas, one spectrum per area, on the sample surface and displayed together to highlight any differences at the surface for the vacuum annealed samples at 300 °C (green) in OAE-1 (Fe 2*p*, Fe 3*p*, and valence band). OAE-2 had spectra collected at two separate areas, one spectrum per area, for all sample surfaces (Fe 2*p* and Fe 3*p*). OAE-1 is represented by a blue box while OAE-2 is represented by an orange box.

with decreasing nanoparticle size (NH40 and NH08, respectively) after vacuum annealing, which suggests that smaller hematite nanoparticles have more Fe(II) at the surface, in agreement with diffraction data.[13] In the case of NH08, the Fe $2p_{3/2}$ peak position (∼710 eV) was consistent with Fe(II)-bearing iron oxides, such as wurtzite ($Fe^{II}O$), and mixed Fe(II)/(III)-nearing iron oxides, such as magnetite (Fe_3O_4),[35,66] and contained a Fe(II) satellite.[67] Similar observations and conclusions were reached regarding the Fe 3*p* spectra (Figure S17). The Fe reduction results align with an XPS study by Lahiri et al.,[10] who attribute an increase in Fe(II) in Fe 3*p* core-level spectra after vacuum annealing due to the presence of oxygen vacancies.

The valence band spectra highlight changes to Fe oxidation state.[10,66] In the valence band spectra of bulk hematite (Figure 4**D**), a small shoulder appeared around 1.5 eV after vacuum annealing, which Minati et al.[66] suggest may be due to the presence of Fe(II) in octahedral coordination. The valence band spectra for NH40 and NH08 show an increasingly large shoulder at lower binding energies with decreasing crystallite size (Figure 4**E**−**F**). These results suggest that there is an increase in Fe(II) species[10] with decreasing crystallite size. Hematite has a band gap of 2.1−2.2 eV,[68] the energy of which can be influenced by crystallite size.[69]

Studies by Lahiri et al.[10] find that oxygen vacancies can form at 300 °C by vacuum annealing and that oxygen vacancies can induce Fe reduction on hematite surfaces. Prior to the vacuum annealing step, the samples underwent an oxygen annealing step (100 mTorr O_2 in 300 °C) to remove adsorbates and carbon.[10] The results show that Fe reduction occurs at the (104) surfaces of 80 nm hematite nanoparticles, but not the (001) surfaces of 200 nm hematite particles or the (012) surfaces of 30 nm hematite nanoparticles.[10] They find that the heating in vacuum led to preferential oxide reduction on the (104) surface and an increase in reactivity. In comparison, our VAC experiments also show that Fe reduction occurred at the surfaces of bulk hematite, NH40, and NH08. However, in Lahiri et al.,[10] the extent of Fe reduction was not as drastic as our experiments which we hypothesize is due to their removal of carbon from sample surfaces in the initial step via oxygen annealing.

Fe reduction follows the trend NH08 > NH40 > Bulk, where Fe reduction is greater at smaller crystallite sizes after vacuum annealing. This size-dependent result has not been reported elsewhere. Here, we observe a correlation between initial crystallite size and oxygen loss after vacuum annealing; Fe reduction occurs more readily on nanoscale surfaces than bulk hematite surfaces. Both the PXRD results (Figure 1 and Table 2) and electron diffraction (Figure 2 and Table 3) show that we have a hematite with magnetite-maghemite in solid solution after vacuum annealing. This phase transformation is direct evidence for oxygen loss because as hematite becomes oxygen deficient (i.e., α-$Fe_2O_{3\text{-}x}$), magnetite/maghemite can form from changes in stoichiometry. Fe reduction after vacuum annealing has been attributed to the creation of oxygen vacancies.[10,13,35] We propose that oxygen vacancy formation is the main mechanism of Fe reduction but also hypothesize that carbon is participating in the reduction by serving as a sink for oxygen removal. Carbonaceous material is known to reduce transition metal oxides, such as copper oxides, during vacuum annealing.[53,70] This is because the oxygen may interact with the surface carbon and create CO_x species, contributing to the oxygen loss in this system.[53] Therefore, due to the increase in carbon concentrations at the surface observed after vacuum annealing treatment (Table S6), an investigation into the effect of carbon on Fe reduction at hematite surfaces was conducted.

Oxygen and Vacuum Annealing Experiments (OAE-1 and OAE-2). Oxygen annealing can remove oxygen vacancies,[10,37,71] and it is also a treatment employed to remove carbon from sample surfaces.[10] To isolate and better understand the role of carbon, we conducted two different oxygen + vacuum annealing experiments (Table 1): OAE-1 served to partially remove carbon off the surface, and OAE-2 removed nearly all of the carbon from the sample surfaces. The atomic percentage of carbon in each sample and sample treatment are provided in Tables S8 and S9, and the survey scans for both OAE-1 and OAE-2 are in Figure S18 and Figure S19, respectively.

The Fe 2*p* core-level spectra, Fe 3*p* core-level spectra, and valence band spectra for NH08 were collected before and after each OAE-1 treatment (Figure 5**A**−**C**). The Fe 2*p* core-level spectra before treatment and after the oxygen annealing step are very similar. Slight shifts to higher binding energies after oxygen annealing may be due to enhanced crystallinity and improvement in crystalline structure.[37] Once the sample was vacuum annealed (to 250 °C and then 300 °C), the intensity of the Fe(III) satellite at 719 eV decreased, which correlates to an increase in Fe(II) species (Figure 5**A**).[13] Further, the Fe $2p_{3/2}$ peak position shifted to 710.5 eV and the Fe $2p_{3/2}$ peak broadened, indicating that Fe reduction occurred. Similar observations were made for the Fe 3*p* core level spectra (Figure 5**B**). The valence band spectra confirm Fe reduction, as indicated by the shifting of the shoulder to lower binding energies after vacuum annealing (Figure 5**C**). Fe reduction was not expected at the lower vacuum annealing temperature (i.e., 250 °C), as previous studies do not report Fe reduction occurring until 300 °C due to oxygen vacancies.[10] Therefore, this is the lowest temperature reported where there was spectroscopically observable Fe reduction on hematite surfaces due to oxygen vacancies under vacuum annealing conditions.

In the second set of oxygen + vacuum annealing experiments (OAE-2), carbon was removed by two oxygen annealing steps and one vacuum annealing step. The resulting Fe 2*p* core-level, Fe 3*p* core-level, and valence band spectra are displayed in Figure 5. The spectra are identical across all three hematite samples (bulk, NH40, and NH08) indicating the lack of Fe reduction (Figure 5**D**−**F**) in the near-absence of carbon (Table S9).

■ CONCLUSIONS

In our VAC results, the carbon atomic concentrations at the surface increased and the amount of Fe(II) present increased with decreasing crystallite size. We hypothesize that the high reactive surface area of NH40 and NH08 (Table S1) enhances the interactions with carbon at the surface, which leads to enhanced oxygen loss in the system at smaller crystallite sizes. Li et al.[72] shows that carbon may take part in the reduction of CuO to Cu_2O by combining with oxygen atoms to form CO_2, which establishes that carbon has an influence on enhancing oxygen loss in copper oxide films. Similar CO_x species are likely forming under our experimental conditions, but in the absence of mass spectrometry data, the extent of CO_x is qualitative. A future investigation that couples XPS with mass spectrometry to monitor gas evolution would make evident the extent of oxygen loss in these systems.

The oxygen + vacuum annealing results show that carbon plays a definitive role in Fe reduction. In the presence of some carbon (OAE-1), Fe reduction occurred, though the amount of Fe reduction was significantly less than in the VAC experiments. In the near-absence of carbon (OAE-2), we did not observe any Fe reduction, regardless of crystallite size. These results show that the presence and amount of carbon is significant, as it serves as a sink for the removed oxygen and enhances oxygen vacancy creation which leads to Fe reduction (under vacuum annealing conditions). Other studies, e.g., by Hensling et al.,[15] also report that contaminants such as CO and H_2 play a role in enhancing oxygen vacancy formation during vacuum annealing. Reductive molecules, such as H_2, can create oxygen vacancies via electron transfer to the surface oxygens.[73] Proton-assisted reactions can also contribute to the creation of oxygen vacancies.[74] We propose that the reactions that produce H_2O are still consistent with hydrocarbon contaminants having a role in the reduction process.[70]

In addition, it is possible that the higher concentrations of Fe(II) were also produced through carbon-mediated reactions, as described by reactions 1 and 2.[70] The proposed carbon-mediated reduction reactions remove oxygen and create oxygen vacancies that facilitate the reduction of hematite to phases along the magnetite-maghemite solid solution.

$$6Fe_2O_3(s) + C(s) \rightarrow 4Fe_3O_4(s) + CO_2(g) \qquad (1)$$

$$3Fe_2O_3(s) + C(s) \rightarrow 2Fe_3O_4(s) + CO(g) \qquad (2)$$

These reactions are also thermodynamically favorable (ΔG at 300 °C = − 75.1 kJ·mol^{-1} and − 2.0 kJ·mol^{-1}, respectively).[70]

As mentioned earlier, a similar study by Lahiri et al.[10] report Fe surface reduction on hematite nanoparticles after vacuum annealing due to oxygen vacancies. Prior to vacuum annealing, Lahiri and team perform an oxygen annealing step that removes surface carbon.[10] In our VAC experiments, we did not remove carbon from the sample surfaces prior to vacuum annealing. The extent of Fe reduction here was greater than the Lahiri et al. study, which we attribute to both oxygen vacancies and carbon serving as a sink for oxygen removal.[10] In addition, their study does not report a size-dependent trend with surface reduction as we observe and report in this study.

This study highlights the importance of interactions between defects and available carbon on surface reactivity. Future work under controlled vacuum annealing conditions (e.g., varying high pressure, higher temperatures) will explore the quantitative nature of the interplay between defects and carbonaceous material, and the effect this has on the reduction of Fe at iron oxide mineral surfaces.

■ ASSOCIATED CONTENT

Supporting Information

The Supporting Information is available free of charge at https://pubs.acs.org/doi/10.1021/acs.jpcc.4c08423.

> PXRD Rietveld refinement details; more electron microscopy (imaging, FFT and electron diffraction); XPS fitting parameters; additional XPS results (survey scans, C 1*s* and Fe 3*p*); atomic quantification (%) tables; crystallite size histograms; BET, pore volume, and crystallite size table (PDF)

AUTHOR INFORMATION

Corresponding Authors

Carolyn I. Pearce − *Pacific Northwest National Laboratory, Richland, Washington 99352, United States;* orcid.org/0000-0003-3098-1615; Email: carolyn.pearce@pnnl.gov

Amy E. Hixon − *University of Notre Dame Department of Civil & Environmental Engineering and Earth Sciences, Notre Dame, Indiana 46556, United States;* orcid.org/0000-0003-4513-4574; Email: ahixon@nd.edu

Authors

Frances E. Zengotita − *University of Notre Dame Department of Civil & Environmental Engineering and Earth Sciences, Notre Dame, Indiana 46556, United States;* orcid.org/0000-0002-7279-4757

Nabajit Lahiri − *Pacific Northwest National Laboratory, Richland, Washington 99352, United States;* orcid.org/0000-0003-1137-2240

Mark H. Engelhard − *Pacific Northwest National Laboratory, Richland, Washington 99352, United States;* orcid.org/0000-0002-5543-0812

Maksym Zhukovskyi − *Notre Dame Integrated Imaging Facility, University of Notre Dame, Notre Dame, Indiana 46556, United States*

Manuel R. Vejar − *University of Notre Dame Department of Civil & Environmental Engineering and Earth Sciences, Notre Dame, Indiana 46556, United States;* orcid.org/0000-0003-4782-2020

Kevin M. Rosso − *Pacific Northwest National Laboratory, Richland, Washington 99352, United States;* orcid.org/0000-0002-8474-7720

Complete contact information is available at:
https://pubs.acs.org/10.1021/acs.jpcc.4c08423

Funding

This material is based on work that is supported by the National Science Foundation under grant no. CHE-1847939. F.E.Z. was funded by the University Nuclear Leadership Program (UNLP) under grant no. DE-FOA-0002265. N.L., M.H.E., K.M.R., and C.I.P. acknowledge support from the U.S. Department of Energy (DOE), Office of Science, Office of Basic Energy Sciences (BES), Chemical Sciences, Geosciences, and Biosciences Division, through its Geosciences Program at Pacific Northwest National Laboratory (PNNL) (FWP #56674). M.R.V. was supported by a National Science Foundation (NSF) Graduate Research Fellowship (Grant No. DGE-1841556). F.E.Z. and M.R.V. acknowledge the GLOBES Graduate Certificate Program in Environment and Society at the University of Notre Dame.This research was performed on a project award 10.46936/lser.proj.2021.51922/60000373 from the Environmental Molecular Sciences Laboratory, a DOE Office of Science User Facility sponsored by the Biological and Environmental Research program under contract no. DE-AC05−76RL01830.

Notes

The authors declare no competing financial interest.

ACKNOWLEDGMENTS

F.E. Zengotita acknowledges Virginia Rodriguez, Kimberly Ruiz Arcineda, and Darian Bridges for their help with nanoparticle syntheses, the Notre Dame Integrated Imaging Facility (NDIIF) for TEM training and usage, and Dr. Allen Oliver for his valuable insight into the research in this work. We freeze-dried our minerals at the Center for Environmental Science and Technology (CEST) at University of Notre Dame. We would like to thank the Molecular Structure Facility at the University of Notre Dame for the use of the PXRD instrument. TOC was created in BioRender. Zengotita, F. (2025) https://BioRender.com/w51z529

ABBREVIATIONS

NP- nanoparticle
TEM- transmission electron microscopy
BE- binding energy
XPS- X-ray photoelectron spectroscopy
PXRD- powder X-ray diffraction
FFT- fast Fourier transform

REFERENCES

(1) Phan, H. T.; Haes, A. J. What Does Nanoparticle Stability Mean? *J. Phys. Chem. C* **2019**, *123* (27), 16495−16507.

(2) Waychunas, G. A.; Zhang, H. Structure, Chemistry, and Properties of Mineral Nanoparticles. *Elements* **2008**, *4* (6), 381−387.

(3) Harish, V.; Tewari, D.; Gaur, M.; Yadav, A. B.; Swaroop, S.; Bechelany, M.; Barhoum, A. Review on Nanoparticles and Nanostructured Materials: Bioimaging, Biosensing, Drug Delivery, Tissue Engineering, Antimicrobial, and Agro-Food Applications. *Nanomaterials* **2022**, *12* (3), 457.

(4) Spielman-Sun, E.; Bland, G.; Wielinski, J.; Frouté, L.; Kovscek, A. R.; Lowry, G. V.; Bargar, J. R.; Noël, V. Environmental Impact of Solution pH on the Formation and Migration of Iron Colloids in Deep Subsurface Energy Systems. *Sci. Total Environ.* **2023**, *902*, No. 166409.

(5) Virot, M.; Dumas, T.; Cot-Auriol, M.; Moisy, P.; Nikitenko, I. S. Synthesis and Multi-Scale Properties of PuO 2 Nanoparticles: Recent Advances and Open Questions. *Nanoscale Adv.* **2022**, *4* (23), 4938−4971.

(6) Waychunas, G. A.; Kim, C. S.; Banfield, J. F. Nanoparticulate Iron Oxide Minerals in Soils and Sediments: Unique Properties and Contaminant Scavenging Mechanisms. *J. Nanoparticle Res.* **2005**, *7* (4−5), 409−433.

(7) Romanchuk, A.; Trigub, A.; Plakhova, T.; Kuzenkova, A.; Svetogorov, R.; Kvashnina, K.; Kalmykov, S. Effective Coordination Numbers from EXAFS: General Approaches for Lanthanide and Actinide Dioxides. *J. Synchrotron Radiat.* **2022**, *29* (2), 288−294.

(8) Madden, A. S.; Hochella, M. F. A Test of Geochemical Reactivity as a Function of Mineral Size: Manganese Oxidation Promoted by Hematite Nanoparticles. *Geochim. Cosmochim. Acta* **2005**, *69* (2), 389−398.

(9) Madden, A. S.; Hochella, M. F.; Luxton, T. P. Insights for Size-Dependent Reactivity of Hematite Nanomineral Surfaces through Cu2+ Sorption. *Geochim. Cosmochim. Acta* **2006**, *70* (16), 4095−4104.

(10) Lahiri, N.; Song, D.; Zhang, X.; Huang, X.; Stoerzinger, K. A.; Carvalho, O. Q.; Adiga, P. P.; Blum, M.; Rosso, K. M. Interplay between Facets and Defects during the Dissociative and Molecular Adsorption of Water on Metal Oxide Surfaces. *J. Am. Chem. Soc.* **2023**, *145*, 2930−2940.

(11) Adegoke, H. I.; AmooAdekola, F.; Fatoki, O. S.; Ximba, B. J. Adsorption of Cr (VI) on Synthetic Hematite (α-Fe2O3) Nanoparticles of Different Morphologies. *Korean J. Chem. Eng.* **2014**, *31* (1), 142−154.

(12) Chernyshova, I. V.; Hochella, M. F. Jr.; Madden, A. S. Size-Dependent Structural Transformations of Hematite Nanoparticles. 1. Phase Transition. *Phys. Chem. Chem. Phys.* **2007**, *9* (14), 1736−1750.

(13) Rioult, M.; Stanescu, D.; Fonda, E.; Barbier, A.; Magnan, H. Oxygen Vacancies Engineering of Iron Oxides Films for Solar Water Splitting. *J. Phys. Chem. C* **2016**, *120* (14), 7482−7490.

(14) da Silva Alvim, R.; Ribeiro, F. N.; Dalpian, G. M. Iron and Oxygen Vacancies at the Hematite Surface: Pristine Case and with a Chlorine Adatom. *Phys. Chem. Chem. Phys.* **2020**, *22* (43), 25380−25389.

(15) Hensling, F. V. E.; Xu, C.; Gunkel, F.; Dittmann, R. Unraveling the Enhanced Oxygen Vacancy Formation in Complex Oxides during Annealing and Growth. *Sci. Rep.* **2017**, 7 (1), 39953.

(16) Wang, L.; Zhu, J.; Liu, X. Oxygen-Vacancy-Dominated Cocatalyst/Hematite Interface for Boosting Solar Water Splitting. *ACS Appl. Mater. Interfaces* **2019**, *11* (25), 22272−22277.

(17) Zvanut, M. E.; Jeddy, S.; Towett, E.; Janowski, G. M.; Brooks, C.; Schlom, D. An Annealing Study of an Oxygen Vacancy Related Defect in SrTiO3 Substrates. *J. Appl. Phys.* **2008**, *104* (6), No. 064122.

(18) Schlueter, C.; Lübbe, M.; Gigler, A. M.; Moritz, W. Growth of Iron Oxides on Ag(111) — Reversible Fe2O3/Fe3O4 Transformation. *Surf. Sci.* **2011**, *605* (23−24), 1986−1993.

(19) Voelz, J. L.; Arnold, W. A.; Penn, R. L. Redox-Induced Nucleation and Growth of Goethite on Synthetic Hematite Nanoparticles. *Am. Mineral.* **2018**, *103* (7), 1021−1029.

(20) Fleet, M. E. The Structure of Magnetite: Symmetry of Cubic Spinels. *J. Solid State Chem. Fr.* **1986**, *62*, 75−82.

(21) Wyckoff, R. W. G. *Crystal Structures*. 2.ed.; Wiley: New York, NY, 1964, Vol. *2*.

(22) Shmakov, A. N.; Kryukova, G. N.; Tsybulya, S. V.; Chuvilin, A. L.; Solovyeva, L. P. Vacancy Ordering in γ-Fe2O3: Synchrotron X-Ray Powder Diffraction and High-Resolution Electron Microscopy Studies. *J. Appl. Crystallogr.* **1995**, *28* (2), 141−145.

(23) Doebelin, N.; Kleeberg, R. Profex: A Graphical User Interface for the Rietveld Refinement Program BGMN. *J. Appl. Crystallogr.* **2015**, *48* (5), 1573−1580.

(24) Schneider, C. A.; Rasband, W. S.; Eliceiri, K. W. NIH Image to ImageJ: 25 Years of Image Analysis. *Nat. Methods* **2012**, *9* (7), 671−675.

(25) Moreau, L. M.; Ha, D.-H.; Zhang, H.; Hovden, R.; Muller, D. A.; Robinson, R. D. Defining Crystalline/Amorphous Phases of Nanoparticles through X-Ray Absorption Spectroscopy and X-Ray Diffraction: The Case of Nickel Phosphide. *Chem. Mater.* **2013**, *25* (12), 2394−2403.

(26) Bang, S.; Russo, D. R.; Knapp, A. D.; Straub, M. D.; Smith, K. F.; Booth, C. H.; Minasian, S. G.; Moreau, L. M. Modeling Heterogeneity in UO2 Nanoparticles Using X-Ray Absorption Spectroscopy. *Eur. J. Inorg. Chem.* **2023**, *26* (7), No. e202200417.

(27) *Characterization of Nanoparticles Intended for Drug Delivery*; McNeil, S. E., Ed.; Methods in Molecular Biology; Humana Press: Totowa, NJ, 2011; Vol. *697*. .

(28) Mourdikoudis, S.; Pallares, R. M.; Thanh, N. T. K. Characterization Techniques for Nanoparticles: Comparison and Complementarity upon Studying Nanoparticle Properties. *Nanoscale* **2018**, *10* (27), 12871−12934.

(29) Chen, S. A.; Heaney, P. J.; Post, J. E.; Eng, P. J.; Stubbs, J. E. Vacancy Infilling during the Crystallization of Fe-Deficient Hematite: An in Situ Synchrotron X-Ray Diffraction Study of Non-Classical Crystal Growth. *Am. Mineral.* **2023**, *108* (9), 1720−1731.

(30) Kishore, V.; Chen, X.; Hassen, A.; Lindahl, J.; Kunc, V.; Duty, C. Effect of Post-Processing Annealing on Crystallinity Development and Mechanical Properties of Polyphenylene Sulfide Composites Printed on Large-Format Extrusion Deposition System. In *SAMPE 2019 - Charlotte, NC*; SAMPE: 2019. .

(31) Arzak, A.; Eguiazábal, J. I.; Nazábal, J. Effect of Annealing on the Properties of Poly(Ether Ether Ketone). *Polym. Eng. Sci.* **1991**, *31* (8), 586−591.

(32) Srithep, Y.; Nealey, P.; Turng, L. Effects of Annealing Time and Temperature on the Crystallinity and Heat Resistance Behavior of Injection-molded Poly(Lactic Acid). *Polym. Eng. Sci.* **2013**, *53* (3), 580−588.

(33) Dang, M.-Z.; Rancourt, D. G.; Dutrizac, J. E.; Lamarche, G.; Provencher, R. Interplay of Surface Conditions, Particle Size, Stoichiometry, Cell Parameters, and Magnetism in Synthetic Hematite-like Materials. *Hyperfine Interact.* **1998**, *117* (1), 271−319.

(34) Gorski, C. A.; Scherer, M. M. Determination of Nanoparticulate Magnetite Stoichiometry by Mossbauer Spectroscopy, Acidic Dissolution, and Powder X-Ray Diffraction: A Critical Review. *Am. Mineral.* **2010**, *95* (7), 1017−1026.

(35) Xue, M.; Wang, S.; Wu, K.; Guo, J.; Guo, Q. Surface Structural Evolution in Iron Oxide Thin Films. *Langmuir* **2011**, *27* (1), 11−14.

(36) Paolone, A.; Angelucci, M.; Panero, S.; Betti, M. G.; Mariani, C. Thermal Stability and Reduction of Iron Oxide Nanowires at Moderate Temperatures. *Beilstein J. Nanotechnol.* **2014**, *5* (1), 323−328.

(37) Pyeon, M.; Ruoko, T.-P.; Leduc, J.; Gönüllü, Y.; Deo, M.; Tkachenko, N. V.; Mathur, S. Critical Role and Modification of Surface States in Hematite Films for Enhancing Oxygen Evolution Activity. *J. Mater. Res.* **2018**, *33* (4), 455−466.

(38) Wang, X.; He, Y.; Liu, L.; Song, D.; Kovarik, L.; Bowden, M. E.; Engelhard, M.; Li, X.; Du, Y.; Miller, Q. R.; Wang, C.; De Yoreo, J. J.; Rosso, K. M.; Zhang, X. Uncovering the Size-Dependent Thermal Solid Transformation of Akaganéite. *Small* **2024**, *20* (46), No. 2402717.

(39) Karim, W.; Kleibert, A.; Hartfelder, U.; Balan, A.; Gobrecht, J.; Van Bokhoven, J. A.; Ekinci, Y. Size-Dependent Redox Behavior of Iron Observed by in-Situ Single Nanoparticle Spectro-Microscopy on Well-Defined Model Systems. *Sci. Rep.* **2016**, *6* (1), 18818.

(40) Wen, Y.; Yunxin, W.; Hai, G. Molecular Dynamics Simulations of the Effects of Annealing on the Micro Residual Stress Induced by Vacancy Defects in Aluminum Crystal. *J. Cryst. Growth* **2020**, *546*, No. 125754.

(41) Folger, A.; Ebbinghaus, P.; Erbe, A.; Scheu, C. Role of Vacancy Condensation in the Formation of Voids in Rutile TiO2 Nanowires. *ACS Appl. Mater. Interfaces* **2017**, *9* (15), 13471−13479.

(42) Zarnas, P. D.; Boyce, B. L.; Qu, J.; Dingreville, R. Stress-Induced Transition from Vacancy Annihilation to Void Nucleation near Microcracks. *Int. J. Solids Struct.* **2021**, *213*, 103−110.

(43) Loginov, Y. Y.; Brown, P. D.; Kovalev, I. V. Formation of Dislocation Loops and Voids in Electron Irradiated Zinc Selenide Single Crystals. *IOP Conf. Ser. Mater. Sci. Eng.* **2017**, *255*, No. 012014.

(44) Blake, R. L.; Hessevick, R. E.; Zoltai, T.; Finger, L. W. Refinement of the Hematite Structure. *Am. Mineral.* **1966**, *51* (1−2), 123−129.

(45) Souza, T. G. F.; Freitas, E. T. F.; Mohallem, N. D. S.; Ciminelli, V. S. T. Defects Induced by Al Substitution Enhance As(V) Adsorption on Ferrihydrites. *J. Hazard. Mater.* **2021**, *420*, No. 126544.

(46) Tigau, N.; Condurache-Bota, S.; Drasovean, R.; Cringanu, J.; Gavrila, R. Vacuum annealing effect on the structural and optical properties of antimony trioxide thin films. *Rom. J. Phys.* **2017**, *62*, 604.

(47) Ji, N.; Chen, Y.; Li, Z.; Wang, J.; Duan, X.; Liu, K.; Jiang, H. Effects of Annealing on the Structures and Properties of Er,Yb:LuGdVO4 Crystal. *Results Phys.* **2019**, *14*, No. 102440.

(48) Lahouli, R.; Massoudi, J.; Smari, M.; Rahmouni, H.; Khirouni, K.; Dhahri, E.; Bessais, L. Investigation of Annealing Effects on the Physical Properties of Ni0.6Zn0.4Fe1.5Al0.5O4 Ferrite. *RSC Adv.* **2019**, *9* (35), 19949−19964.

(49) Jafari, A.; Farjami Shayesteh, S.; Salouti, M.; Boustani, K. Effect of Annealing Temperature on Magnetic Phase Transition in Fe3O4 Nanoparticles. *J. Magn. Magn. Mater.* **2015**, *379*, 305−312.

(50) Tang, Y.; Qin, H.; Wu, K.; Guo, Q.; Guo, J. The Reduction and Oxidation of Fe2O3(0001) Surface Investigated by Scanning Tunneling Microscopy. *Surf. Sci.* **2013**, *609*, 67−72.

(51) Ahn, Y.; Kim, J.; Ganorkar, S.; Kim, Y.-H.; Kim, S.-I. Thermal Annealing of Graphene to Remove Polymer Residues. *Mater. Express* **2016**, *6* (1), 69−76.

(52) Al-Ajlony, A.-M. B.; Kanjilal, A.; Harilal, S. S.; Hassanein, A. Carbon Contamination and Oxidation of Au Surfaces under Extreme Ultraviolet Radiation: An x-Ray Photoelectron Spectroscopy Study. *J. Vac. Sci. Technol. B Nanotechnol. Microelectron. Mater. Process. Meas. Phenom.* **2012**, *30* (4), No. 041603.

(53) Lee, S. Y.; Mettlach, N.; Nguyen, N.; Sun, Y. M.; White, J. M. Copper Oxide Reduction through Vacuum Annealing. *Appl. Surf. Sci.* **2003**, *206* (1−4), 102−109.

(54) Grey, L. H.; Nie, H.-Y.; Biesinger, M. C. Defining the Nature of Adventitious Carbon and Improving Its Merit as a Charge Correction Reference for XPS. *Appl. Surf. Sci.* **2024**, *653*, No. 159319.

(55) Comini, N.; Huthwelker, T.; Diulus, J. T.; Osterwalder, J.; Novotny, Z. Factors Influencing Surface Carbon Contamination in Ambient-Pressure x-Ray Photoelectron Spectroscopy Experiments. *J. Vac. Sci. Technol. A* **2021**, *39* (4), No. 043203.

(56) Greczynski, G.; Hultman, L. Impact of Sample Storage Type on Adventitious Carbon and Native Oxide Growth: X-Ray Photoelectron Spectroscopy Study. *Vacuum* **2022**, *205*, No. 111463.

(57) Mattevi, C.; Eda, G.; Agnoli, S.; Miller, S.; Mkhoyan, K. A.; Celik, O.; Mastrogiovanni, D.; Granozzi, G.; Garfunkel, E.; Chhowalla, M. Evolution of Electrical, Chemical, and Structural Properties of Transparent and Conducting Chemically Derived Graphene Thin Films. *Adv. Funct. Mater.* **2009**, *19* (16), 2577−2583.

(58) Wu, Y.; Li, H.; Ji, L.; Liu, L.; Ye, Y.; Chen, J.; Zhou, H. Effect of Vacuum Annealing on the Microstructure and Tribological Behavior of Hydrogenated Amorphous Carbon Films Prepared by Magnetron Sputtering. *Proc. Inst. Mech. Eng. Part J. J. Eng. Tribol.* **2013**, *227* (7), 729−737.

(59) Gengenbach, T. R.; Major, G. H.; Linford, M. R.; Easton, C. D. Practical Guides for X-Ray Photoelectron Spectroscopy (XPS): Interpreting the Carbon 1s Spectrum. *J. Vac. Sci. Technol. A* **2021**, *39* (1), No. 013204.

(60) Blume, R.; Rosenthal, D.; Tessonnier, J.; Li, H.; Knop-Gericke, A.; Schlögl, R. Characterizing Graphitic Carbon with X-ray Photoelectron Spectroscopy: A Step-by-Step Approach. *ChemCatChem.* **2015**, *7* (18), 2871−2881.

(61) Morgan, D. J. Comments on the XPS Analysis of Carbon Materials. *C* **2021**, *7* (3), 51.

(62) Gonzalez-Elipe, A. R.; Espinos, J. P.; Fernandez, A.; Munuera, G. XPS Study of the Surface Carbonation/Hydroxylation State of Metal Oxides. *Appl. Surf. Sci.* **1990**, *45* (2), 103−108.

(63) Rheinheimer, V.; Unluer, C.; Liu, J.; Ruan, S.; Pan, J.; Monteiro, P. J. M. XPS Study on the Stability and Transformation of Hydrate and Carbonate Phases within MgO Systems. *Materials* **2017**, *10* (1), 75.

(64) Stoch, J.; Gablankowska-Kukucz, J. The Effect of Carbonate Contaminations on the XPS O 1s Band Structure in Metal Oxides. *Surf. Interface Anal.* **1991**, *17* (3), 165−167.

(65) Dillip, G. R.; Banerjee, A. N.; Anitha, V. C.; Deva Prasad Raju, B.; Joo, S. W.; Min, B. K. Oxygen Vacancy-Induced Structural, Optical, and Enhanced Supercapacitive Performance of Zinc Oxide Anchored Graphitic Carbon Nanofiber Hybrid Electrodes. *ACS Appl. Mater. Interfaces* **2016**, *8* (7), 5025−5039.

(66) Minati, L.; Micheli, V.; Rossi, B.; Migliaresi, C.; Dalbosco, L.; Bao, G.; Hou, S.; Speranza, G. Application of Factor Analysis to XPS Valence Band of Superparamagnetic Iron Oxide Nanoparticles. *Appl. Surf. Sci.* **2011**, *257* (24), 10863−10868.

(67) Fujii, T.; de Groot, F. M. F.; Sawatzky, G. A.; Voogt, F. C.; Hibma, T.; Okada, K. In Situ XPS Analysis of Various Iron Oxide Films Grown by ${\mathrm{NO}}_{2}$-Assisted Molecular-Beam Epitaxy. *Phys. Rev. B* **1999**, *59* (4), 3195−3202.

(68) Katsuma, D.; Khoo, P. L.; Kobayashi, M.; Shinagawa, T.; Izaki, M. Structural and Magnetic Characteristics of Hematite and Magnetite Films Prepared by Electrodeposition and Heating. *J. Electrochem. Soc.* **2022**, *169* (4), No. 042501.

(69) Sharma, M.; Murugavel, S.; Shukla, D. K.; De Groot, F. M. F. Reversal in the Lattice Contraction of α-Fe2O3 Nanoparticles. *J. Phys. Chem. C* **2018**, *122* (17), 9292−9301.

(70) Cochran, S. J.; Larkins, F. P. Surface Reduction of Some Transition-Metal Oxides. An X-Ray Photoelectron Spectroscopic Study of Iron, Cobalt, Nickel and Zinc Oxides. *J. Chem. Soc. Faraday Trans. 1 Phys. Chem. Condens. Phases* **1985**, *81* (9), 2179−2190.

(71) Hsu, C.-H.; Geng, X.-P.; Wu, W.-Y.; Zhao, M.-J.; Huang, P.-H.; Zhang, X.-Y.; Su, Z.-B.; Chen, Z.-R.; Lien, S.-Y. Effect of Oxygen Annealing Temperature on Properties of Spatial Atomic Layer Deposited Aluminum-Doped Zinc Oxide Films. *Mater. Sci. Semicond. Process.* **2021**, *133*, No. 105929.

(72) Li, J.; Vizkelethy, G.; Revesz, P.; Mayer, J. W.; Matienzo, L. J.; Emmi, F.; Ortega, C.; Siejka, J. Influence of Carbon on the Enhanced Oxygen Loss in Copper Oxide Films. *Appl. Phys. Lett.* **1991**, *58* (12), 1344−1346.

(73) Zhuang, G.; Chen, Y.; Zhuang, Z.; Yu, Y.; Yu, J. Oxygen Vacancies in Metal Oxides: Recent Progress towards Advanced Catalyst Design. *Sci. China Mater.* **2020**, *63* (11), 2089−2118.

(74) Mofarah, S. S.; Adabifiroozjaei, E.; Yao, Y.; Koshy, P.; Lim, S.; Webster, R.; Liu, X.; Khayyam Nekouei, R.; Cazorla, C.; Liu, Z.; Wang, Y.; Lambropoulos, N.; Sorrell, C. C. Proton-Assisted Creation of Controllable Volumetric Oxygen Vacancies in Ultrathin CeO2-x for Pseudocapacitive Energy Storage Applications. *Nat. Commun.* **2019**, *10* (1), 2594.